THE JOURNAL OF PHYSICAL CHEMISTRY LETTERS
A JOURNAL OF THE AMERICAN CHEMICAL SOCIETY

pubs.acs.org/JPCL

Letter

Coherent Vibrational Dynamics of $Au_{144}(SC_8H_9)_{60}$ Nanoclusters

William R. Jeffries, Sami Malola, Marcus A. Tofanelli, Christopher J. Ackerson, Hannu Häkkinen, and Kenneth L. Knappenberger, Jr.*

Cite This: *J. Phys. Chem. Lett.* 2023, 14, 6679−6685

Read Online

ACCESS | Metrics & More | Article Recommendations | Supporting Information

ABSTRACT: The coherent vibrational dynamics of $Au_{144}(SC_8H_9)_{60}$, obtained from femtosecond time-resolved transient absorption spectroscopy, are described. Two acoustic modes were identified and assigned, including 2.0 THz breathing and 0.7 THz quadrupolar vibrations. These assignments are consistent with predictions using classical mechanics models, indicating that bulk models accurately describe the vibrational properties of $Au_{144}(SC_8H_9)_{60}$. Coherent phonon signals were persistent for up to 3 ps, indicating energy dissipation by the nanocluster was the primary dephasing channel. The initial excitation phases of the breathing and quadrupolar modes were π-phase-shifted, reflecting differences in the displacive nuclear motion of the vibrations. The combined agreement of the vibrational frequencies, relative phases, and decoherence times supported predictions based on classical models. The vibrational frequencies were insensitive to silver substitution for gold but did show increased inhomogeneous damping of the coherent phonons. The ability to predict the vibrational properties of metal nanoclusters can have an impact on nanoresonator and mass sensing technologies.

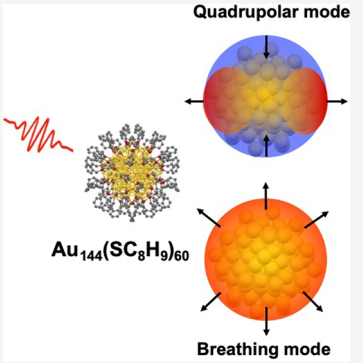

The optical, electronic, and mechanical properties of metal nanoparticles and nanoclusters provide many exciting opportunities for both fundamental and applied research. The mechanical properties of metal colloids have potential implications for nanomechanical resonators and mass and chemical sensing.[1−4] For metal nanoparticles, the acoustic modes are accurately described using classical continuum models that account for displacive lattice motion resulting from coherent phonon excitation.[5−8] It has recently been shown that these models accurately extend to include the low-frequency vibrations of ligand-protected nanoclusters with diameters as small as ∼9 Å and up to 4 nm.[9] Still, other researchers have invoked molecular-like wavepacket models to account for low-frequency ∼1 THz vibrations of nanoclusters in the few-nanometer size range.[10−12] Therefore, research addressing the coherent vibrational dynamics of structurally well-defined condensed-phase ligand-protected metal nanoclusters in the few-nanometer range is needed to understand the mechanical properties of nanometals.

Monolayer-protected clusters (MPCs) are a class of colloidal nanoclusters that are especially well suited for developing nanometal structure−property correlations.[13] MPCs afford a high degree of structural specificity through the formation of so-called magic sizes that can be isolated based on combinations of electronic and geometric considerations. The $Au_{144}(SC_8H_9)_{60}$ MPC is of particular interest for understanding nanometal properties, because it is considered intermediate to the molecular and metallic scales. For example, $Au_{144}(SC_8H_9)_{60}$ exhibits electrochemical charging behavior consistent with a metallic nanoparticle.[14] Following 400 nm excitation, $Au_{144}(SC_8H_9)_{60}$ electronic relaxation dynamics are consistent with two-temperature models for metallic electron gases.[15−17] Similar electronic thermalization times to those from excitation at 400 nm were also observed in $Au_{144}(SC_8H_9)_{60}$ following 652 nm excitation, suggesting metallic behavior.[18] However, the variable-temperature magneto-optical properties of $Au_{144}(SC_8H_9)_{60}$ are clearly distinct from those of metallic or plasmon-supporting nanoparticles.[19,20] Powder X-ray diffraction of $Au_{144}(SC_8H_9)_{60}$ suggests that both metallic (fcc crystallites) and nonmetallic icosahedral polymorphs can be formed.[21] Temperature-dependent single-crystal X-ray diffraction data show a nonmetallic structure for $Au_{144}(SC_8H_9)_{60}$.[22] The 144 gold atoms are divided into a 114-gold-atom core and 30 S−Au−S metal chalcogenide semiring motifs.[23,24] The 114-gold-atom core is further divided into three layers that include a 12-atom icosahedron followed by a second layer of 42 atoms and finally a 60-atom third layer. The 30 S−Au−S motifs distributed on the core induce a chiral pattern on the MPC with an approximately spherical 1.8 nm inorganic diameter. Hence, $Au_{144}(SC_8H_9)_{60}$ is an ideal candidate for understanding the vibrational properties of ligand-protected metal nanoclusters in the few-nanometer range.

Here, we describe femtosecond time-resolved transient absorption spectroscopy measurements of the coherent

Received: May 29, 2023
Accepted: July 12, 2023
Published: July 18, 2023

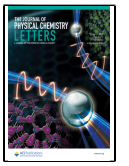

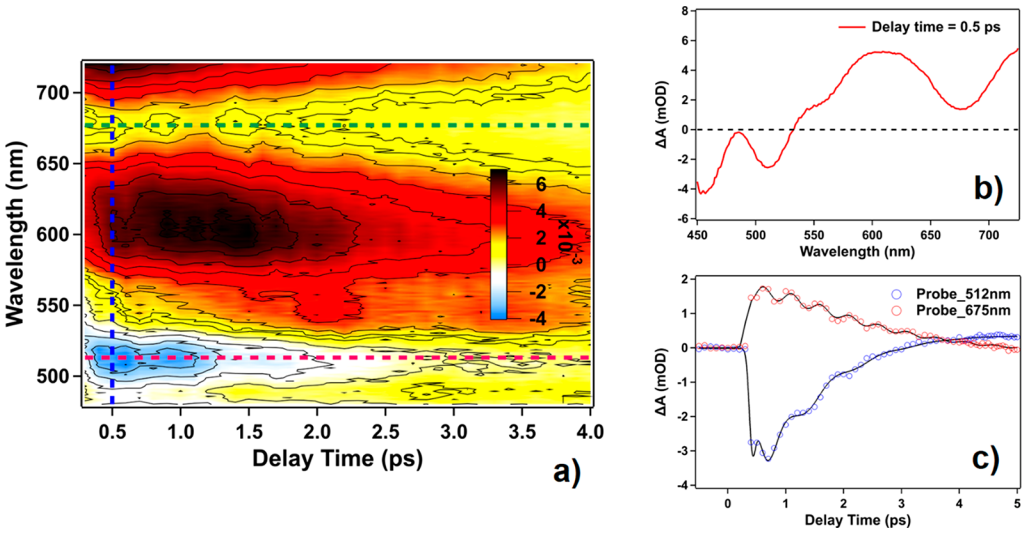

Figure 1. (a) 2D transient absorption contour map obtained for $Au_{144}(SC_8H_9)_{60}$ following excitation by 800 nm light. The detection spectrum spanned the range from 480 to 720 nm; the time domain response is plotted from 0.2 to 4.0 ps. Warm colors (positive amplitude Δ abs) correspond to excited state absorption (ESA), and the cool colors (negative amplitude Δ abs) correspond to ground-state bleach (GSB) signals. (b) Transient absorption spectrum obtained at a pump−probe delay time of 0.5 ps. The global spectrum includes a broad ESA signal superimposed with four distinguishable GSB components located at center wavelengths of 460, 515, 560, and 675 nm. (c) Time-dependent amplitudes of the GSB peaks at 515 (blue open circles) and 675 nm (red open circles). The time-domain transient signals included periodic intensity recurrences that corresponded to coherent acoustic vibrational dynamics. The black lines represent fitting of the experimental data. Data acquired using 800 nm, 1 μJ/pulse excitation.

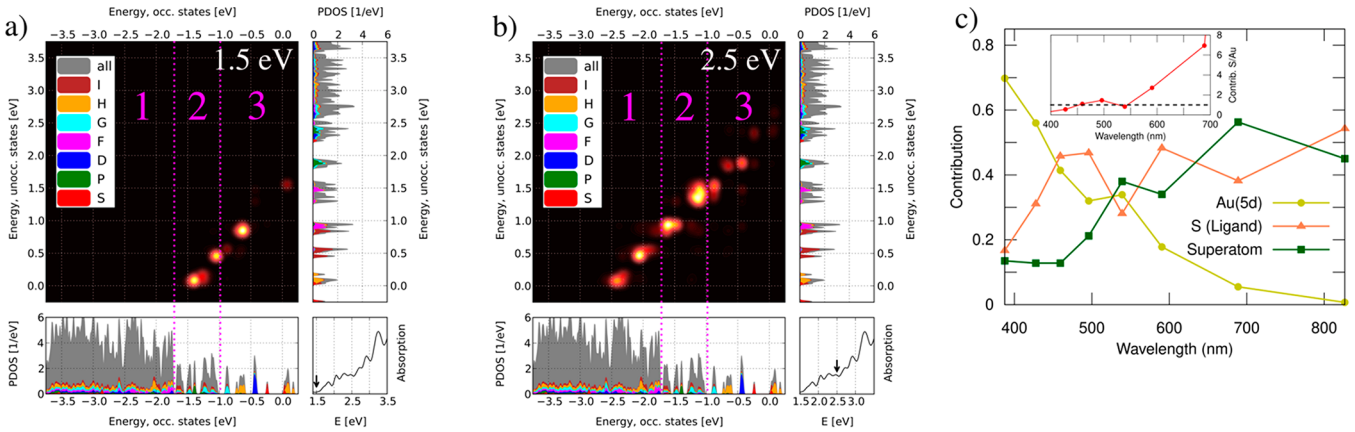

Figure 2. Summary of computational descriptions of the $Au_{144}(SR)_{60}$ excitation spectrum. (a, b) Time-dependent density functional theory (TDDFT) calculations and the transition contribution map (TCM) analysis for the absorption peaks at (a) 1.5 and (b) 2.5 eV (labeled by arrows in the lower right subpanels). The strength of important electron−hole excitations with respect to occupied (lower left subpanels) and unoccupied (upper right subpanels) Kohn−Sham states is shown as a bright yellow color in the contour plot. Magenta numbers 1, 2, and 3 designate energy levels with primary contributions from Au(5d), ligand/S, and superatom states, respectively. Coloring in the projected density of states denotes different angular momenta of the spherical harmonics functions that are used to analyze the superatom characteristics. The band of S and H states just above the numerically determined Fermi energy is partially occupied. (c) Summary of the relative contributions of Au(5d), ligand/S, and superatomic states to absorption transitions in the visible range studied experimentally in this work. A ratio of the relative contribution between ligand/S and Au(5d) is plotted versus excitation wavelength in the inset. The comparison shows that, as the transition wavelength becomes longer, the contribution from the ligand/S component becomes dominant.

vibrational dynamics of $Au_{144}(SC_8H_9)_{60}$ excited by 800 nm light. Our results are fully consistent with classical continuum mechanics descriptions that predict symmetric breathing and antisymmetric quadrupolar acoustic vibrations of the nanocluster.

The experimental layout is presented in Figure S1. The temporally and spectrally resolved transient absorption signals obtained for $Au_{144}(SC_8H_9)_{60}$ following 800 nm excitation (1 μJ/pulse) are summarized in Figure 1. A global view of the transient spectra spanning 450−780 nm probe wavelengths and 0.2−4.0 ps pump−probe time delays is portrayed in Figure 1a. Periodic amplitude recurrences persisting on the picosecond time scale were pervasive in the transient signal (Figure 1a). The transient absorption spectrum obtained at a pump−probe time delay of 0.5 ps is shown in Figure 1b. The Figure 1b spectrum agreed well with our previous results obtained from 400 nm excitation of $Au_{144}(SC_8H_9)_{60}$.[15] The majority of the transient signal resulted from spectrally broad excited state absorption (ESA) that spanned the detection range. However, four distinct transient bleach signals were observed super-

https://doi.org/10.1021/acs.jpclett.3c01477
J. Phys. Chem. Lett. 2023, 14, 6679−6685

imposed on the ESA. The four bleach signals had center detection wavelengths of 460, 512, 560, and 675 nm and are referred to as GSB-460, GSB-512, GSB-560, and GSB-675, hereafter. These bleach signals agreed well with the linear absorption spectra (Figure S2), which showed peaks at 465, 525, 563, and 689 nm. A comparison of the dynamics recorded for GSB-512 and GSB-675 is given in Figure 1c, which shows that the periodic transient absorption intensity recurrences persisted for at least 3 ps. The picosecond persistence of the oscillating signal is consistent with the excitation of coherent acoustic vibrational modes.[5,6] Another important observation is that the vibrational period depended on the detection wavelength; higher frequency oscillations were detected for GSB-675 than for GSB-512.

The origin of the transient bleach components was investigated using time-dependent density functional theory (TDDFT) calculations and transition contribution map (TCM) analysis for $Au_{144}(SR)_{60}$. The TCMs for 825 nm (1.5 eV) and 500 nm (2.5 eV) transitions are shown in Figures 2a and 2b, respectively. The transitions in the visible wavelength range included three major components, which originated from (i) Au(5d), (ii) sulfur/ligand, and (iii) superatom states. Additional details of the calculations and PDOS transition plots are provided in the Supporting Information (Table S1, Figures S3 and S4). As shown in Figure 2c, two general trends are apparent from the calculated TCMs. First, the contribution from Au(5d) transitions increased from less than 1% to almost 70% of the spectral weight as the transition wavelength decreased. Second, the contribution from S atoms decreased from more than 50% to less than 20% as the transition wavelength decreased. The relative contributions of sulfur-based transitions to Au(5d) transitions are plotted in the Figure 2c inset. A clear increase in S-based contributions occurred for wavelengths shorter than ~560 nm. The results suggested that transient bleach signals acquired at wavelengths shorter than ~560 nm resulted from probing Au(5d) transitions, whereas those measured at wavelengths longer than ~560 nm carried significant contributions from sulfur/ligand states.

In order to analyze the properties of the acoustic modes, we isolated the coherent transient signals from those resulting from incoherent population decay. This was accomplished by fitting the data using a multiexponential function

$$\Delta A(t) = A_0 + \sum_i \left(\frac{A_i}{k_i}\right) \mathrm{ExpGauss}(t - t_0, k_i, \sigma) \quad (1)$$

where A_0 is the dc amplitude offset, A_i is the amplitude, k_i is the relaxation rate for the ith signal decay component, respectively, t is the delay time between pump and probe pulses, t_0 is the time zero when the pump and probe pulses arrived at the sample simultaneously, and σ is the width of the Gaussian function used to describe the instrumental response function (IRF). The ExpGauss function represents the convolution of an exponential decay function with the Gaussian (IRF). The signal amplitude was divided by k_i in order to normalize the signals to unit area rather than to unit height. The incoherent electronic relaxation rates obtained from fitting the Figure 3c data using eq 1 yielded three similar time constants for both the GSB-512 and GSB-675 signals. These included an approximate 250 fs growth and a subsequent 1 ps decay. These two time constants are attributed to electron−electron scattering (250 fs) and picosecond electron−lattice (i.e., electron−phonon scattering) heating. The electron−lattice heating is consistent with our previous reports that employed 400 nm excitation of $Au_{144}(SR)_{60}$.[15,17] A third, low-amplitude decay of approximately 3 ps was also used to fit the incoherent time-domain data. Next, the incoherent components retrieved from this fitting were subtracted from the total signal, leaving a residual trace that contained only signatures of the coherent acoustic vibrations.

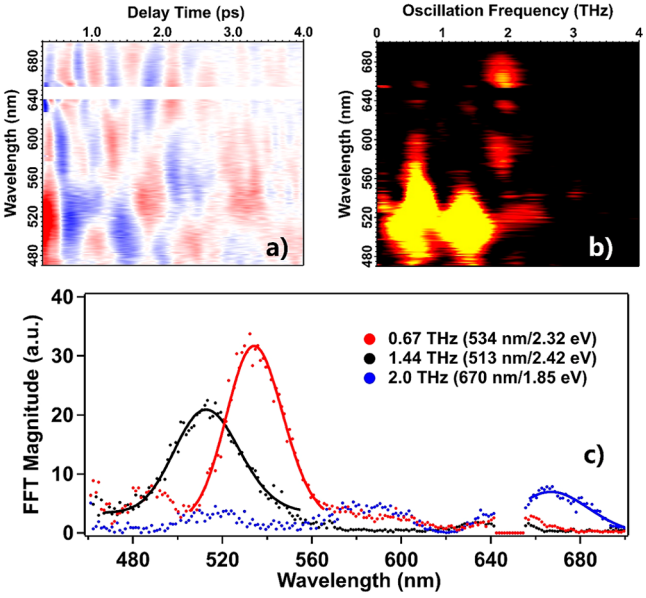

Figure 3. Summary of coherent vibrational dynamics for $Au_{144}(SC_8H_9)_{60}$. (a) 2D plot of the coherent transient signals, obtained by removal of the incoherent signals from Figure 1a. Periodic intensity recurrences are clearly evident in the coherent transient signals. (b) 2D Fourier spectra obtained from the panel a data. Three distinguishable vibrational frequencies corresponding to two modes were identified; the frequencies were 0.7, 1.4, and 2.0 THz. The 2D Fourier spectra showed a clear probe-wavelength dependence, with the low-frequency modes detected at probe wavelengths less than 560 nm and the high-frequency signal dominant at wavelengths longer than 560 nm. The 1.4 THz signal is the harmonic of the 0.7 THz mode. (c) Fourier line spectra for the 2 THz (blue), 1.4 THz (black), and 0.7 THz (red) signal shown in panel b. The low-frequency modes are detected with larger amplitude than the 2.0 THz signal; the 0.7 THz response is the dominant signal. The 0.7 and 2.0 THz signals are assigned to the quadrupolar and breathing modes, respectively, as described in the main text. The 2.0 THz signal is assigned to the nanocluster breathing mode. Data acquired using 800 nm, 1 μJ/pulse excitation.

A global plot of the temporally and spectrally resolved coherent signals (incoherent data removed) is shown in Figure 3a. Note, a stimulated Raman signal from solvent C−H stretching was manually removed at 650 nm. The high frequency mode detected for GSB-675 is observable in the probe wavelength range of 560−700 nm. The period of the mode was approximately 0.5 ps. A lower-frequency mode with an approximate 1.5 ps period was detected at probe wavelengths shorter than 560 nm. To assign frequencies to the coherent vibrations, the Figure 3a time-domain data was Fourier transformed to the frequency domain. The 2D map in Figure 3b plots the resultant Fourier spectra obtained at each probe wavelength. Three distinct vibrational frequencies are shown in Figure 3b. These include a 2.0 THz mode, which is most prominently detected at approximately 670 nm but has nonzero amplitude over most of the probe spectrum and two

https://doi.org/10.1021/acs.jpclett.3c01477
J. Phys. Chem. Lett. 2023, 14, 6679−6685

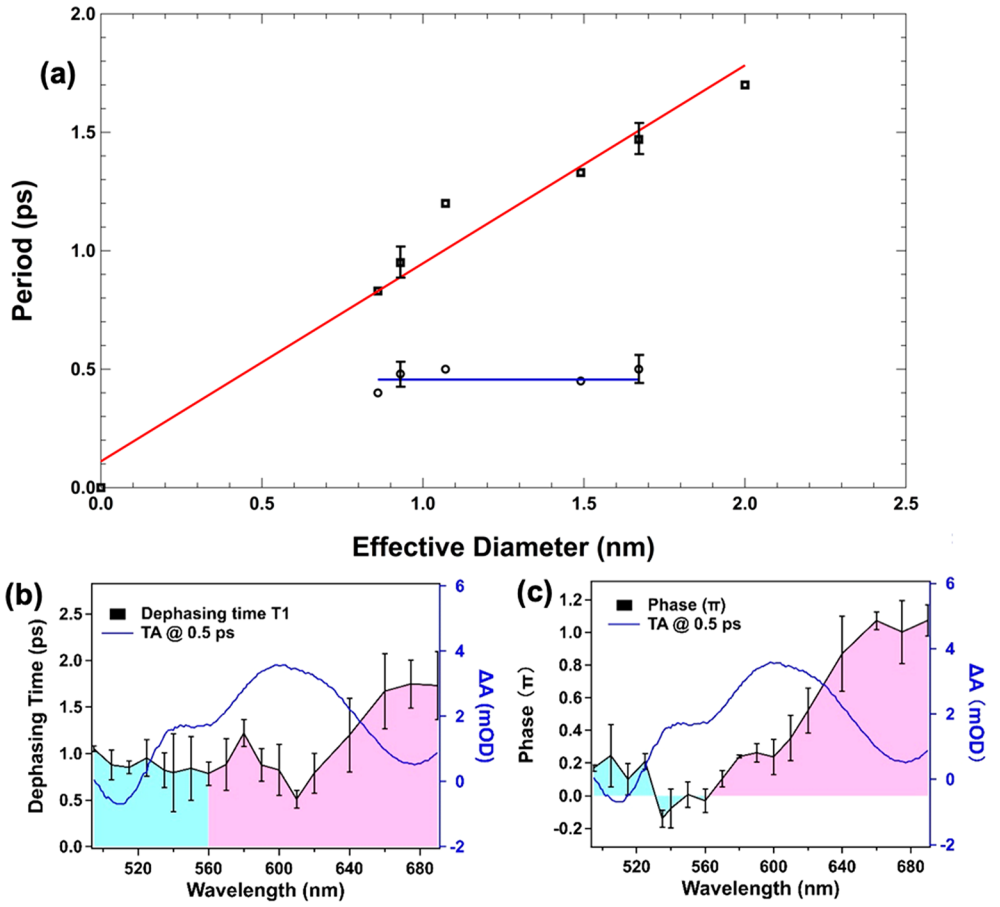

Figure 4. (a) Summary of gold-monolayer-protected cluster (MPC) quadrupolar (□) and breathing mode (○) vibrational frequencies. The vibrational period of a series of MPCs plotted versus nanocluster equivalent diameter, D_{eq}; equivalent diameters spanned the range from 0.86 to 2.0 nm. The plot includes data from $Au_{20}(SR)_{16}$ (D_{eq} = 0.86),[8] $Au_{25}(SC_8H_9)_{18}$ (D_{eq} = 0.95), $Au_{38}(SR)_{24}$ (D_{eq} = 1.2),[21] $Au_{102}(SR)_{44}$ (D_{eq} = 1.33),[7] $Au_{144}(SC_8H_9)_{60}$ (D_{eq} = 1.67), and $Au_{246}(pMBA)_{80}$ (D_{eq} = 2.00).[9] The $Au_{25}(SC_8H_9)_{18}$ and $Au_{144}(SC_8H_9)_{60}$ data were acquired in our laboratory. Error bars are provided for the data collected in this research. Values for other clusters were obtained from the literature as noted. A clear linear dependence of the quadrupolar vibrational period on the equivalent diameter is apparent. An average size-independent breathing mode vibrational period of 0.45 ps was obtained for the nanocluster series. (b, c) Analysis of the coherent time-domain data. Results are overlaid with the probe-wavelength-resolved transient absorption spectra to distinguish responses from quadrupolar (cyan) and breathing (magenta) acoustic modes. (b) Summary of the dephasing lifetime for the coherent vibrations. Lifetimes exceeding 1 ps, consistent with the long persistence of the periodic intensity recurrences shown in Figures 1c and 3a, confirm damping of the acoustic modes by energy dissipation of $Au_{144}(SC_8H_9)_{60}$. (c) Plot of the excitation phase versus probe detection wavelength. The reported phase values correspond to the dominant mode for each probe wavelength. A relative π-phase shift is observed between quadrupolar and breathing mode excitation. The breathing mode exhibits successive in-phase (symmetric) expansion and contraction. Excitation of the quadrupolar modes induces expansion in one direction, that is, out-of-phase with motion in the perpendicular direction, leading to the relative phase shift observed in the time-domain data. The difference in the excitation phase for the breathing and quadrupolar modes suggests these coherent vibrations are excited by distinct mechanisms, as described in the main text. Data acquired using 800 nm, 1 μJ/pulse excitation.

lower frequency signals of 0.7 and 1.4 THz detected for wavelengths shorter than 650 nm. The 1.4 THz signal is assigned as the harmonic of the 0.7 THz mode. In addition to appearing at 2× the frequency of 0.7 THz, the 1.4 THz signal replicates the spectral profile, with slight narrowing of the fundamental. Additional evidence supporting the assignment of the 1.4 THz mode as a harmonic is obtained from pump−probe measurements following silver doping of the cluster. The global coherent signals of $Ag_xAu_{144-x}(SC_8H_9)_{60}$ ($x \approx 30$) are shown in Figure S5a, and the 2D map of the Fourier spectra is given in Figure S5b. Both the 0.7 and 2.0 THz signals were retained upon Ag substitution, but the 1.4 THz mode was not recovered. This could be understood from increased sample inhomogeneity upon Ag substitution for Au at the nanocluster core, which causes more rapid dephasing and reduced amplitude of the coherent recurrences.[17] Hence, the harmonic signal was lost due to increased sample polydispersity.

The acoustic modes of ligand-protected gold nanoclusters, including MPCs, have been studied both theoretically and experimentally by Maioli et al.[9] Although their study spanned nanocluster diameters ranging from <1 to 4 nm, $Au_{144}(SC_8H_9)_{60}$ was not included in their series. For approximately spherical nanoclusters in the few-nanometer size range, such as $Au_{144}(SC_8H_9)_{60}$, two acoustic modes are predicted.[9] A size-independent breathing mode resulting from symmetric dilation of the nanocluster is predicted at a frequency of 2 THz. The Fourier spectra obtained for wavelengths longer than 560 nm (Figure 3b) provided excellent agreement with this prediction. Femtosecond time-resolved transient absorption measurements were also performed on $Au_{25}(SC_8H_9)_{18}$ to confirm the size independence

https://doi.org/10.1021/acs.jpclett.3c01477
J. Phys. Chem. Lett. 2023, 14, 6679−6685

of the high-frequency mode. A 2.0 THz signal was also measured for the $Au_{25}(SC_8H_9)_{18}$ nanocluster (Figure S5). Hence, the 2.0 THz mode shown in Figure 3 for $Au_{144}(SC_8H_9)_{60}$ is assigned to the MPC breathing mode. For most metal nanoparticles, acoustic mode frequencies are expected to increase linearly with inverse radius ($1/R$). Therefore, the size independence of the breathing mode is, at first, surprising. This correlation is sometimes referred to as the elastic frequency law (EFL).[25] However, theoretical modeling predicts a breakdown of EFL models for gold nanocluster breathing modes for systems of fewer than approximately 250 metal atoms.[25,26] Our data as well as those from other researchers are consistent with this prediction. The deviation from EFL predictions is attributed to surface relaxation effects, with smaller wavelength (higher frequency) modes being more sensitive to these effects than longer wavelength (lower frequency) ones. Hence, the quadrupolar mode is predicted to follow the EFL models.

Next, the size-dependent quadrupolar mode is also discussed. For spherical (or nearly spherical) systems, the quadrupolar mode vibrational period is predicted to increase linearly with increasing effective nanocluster equivalent diameter, D_{eq}. The equivalent diameter of an MPC is defined as $D_{eq} = d_0 n^{1/3}$, where n is the number of gold atoms, $d_0 = a[3/(2\pi)]^{1/3}$, and a = 0.408 nm; a is the fcc lattice cubic side.[9] The equivalent diameter is introduced to account for effects of the ligand shell on the nanocluster vibrational frequency. The quadrupolar mode is also expected to be out of phase with the radially symmetric breathing mode. This can be understood by the periodic shape changes resulting from quadrupolar mode excitation; periodic expansion and contraction in one direction is out of phase with respect to this motion in the perpendicular direction.

In order to determine if the 0.7 THz acoustic vibrations of $Au_{144}(SC_8H_9)_{60}$ could be assigned to a quadrupolar mode, the low-frequency vibrational periods obtained for several MPCs in the 0.9−2.0 nm diameter range were compared (Figure 4a). The $Au_{25}(SC_8H_9)_{18}^-$ and $Au_{144}(SC_8H_9)_{60}$ data were collected in our laboratory, and the $Au_{20}(SCH_2CH_2Ph)_{16}$,[10] $Au_{38}(SC_2H_4Ph)_{24}$,[27] $Au_{102}(SPhCOOH)_{44}$,[9] and $Au_{246}(pMBA)_{80}$[11] values were obtained from the literature, as noted. The Figure 4 data showed a clear linear relationship (red line) between the acoustic mode vibrational period and MPC equivalent diameter. The linear trend is especially convincing, given that the data points were obtained from multiple laboratories and researchers. In contrast, the breathing mode vibrational periods were independent of nanocluster equivalent diameter, with an average value of 0.45 ps (blue line). The number of Au atoms, equivalent diameters, vibrational periods, and frequencies for all of the Figure 4a data are summarized in Table S2. The Figure 4 results provide strong support for assignments of the 0.7 THz mode of $Au_{144}(SC_8H_9)_{60}$ to a coherent acoustic quadrupolar mode and the 2.0 THz vibration to an acoustic breathing mode.

Additional analysis of the acoustic modes was performed by modeling the coherent residual time-domain signals using a damped sinusoidal function $I(t) = \sum_i (A_i \cdot e^{-t/t1_i} \cdot \sin(\frac{2\pi t}{t2_i} + \varphi_i))$, where the dephasing lifetime was described using $t1_i$, $t2_i$ was the oscillation period, and φ_i was the initial phase. The subscript i denotes the individual components taken into account for the total coherent signal. In the range of 500−560 nm probe wavelength, a two-component sinusoidal function was used to fit the coherence data (fundamental and harmonic), while a single-component one was employed for residual oscillation dynamics at wavelengths longer than 560 nm. The decoherence times, $t1$, are given in Figure 4b, plotted versus the probe detection wavelength. The decoherence times are generally in the range between 1.0 and 1.75 ps and show only minor variation across the probe wavelength range. Decoherence $1/e$ lifetimes of up to 1.75 ps are consistent with the Figure 3 data that show coherent intensity recurrences persisting for more than 3 ps. The observation of long-lived and probe-wavelength-independent coherence times is consistent with the dephasing of metal nanocluster phonon modes. The dephasing time is determined by energy dissipation rates of the system.[5,6] For $Au_{144}(SC_8H_9)_{60}$, energy dissipation from the nanocluster to the surrounding occurs in the 1−10 ps range, in good agreement with the dephasing times reported here. The decoherence behavior observed for the nanoclusters is in contrast to dephasing of molecular vibrational wavepackets, for which coherence dephasing times are frequently determined by the state-specific lifetimes and relative amplitudes of the various eigenstates that form the coherent superposition.[28,29] For condensed-phase molecules, these lifetimes are often on the time scale of internal conversion (≈100 fs) or dissociation. Still, several examples of molecular wavepackets persisting on picosecond and longer time scales are available.[30] However, time-domain signals of molecular vibrational wavepackets typically carry signatures of a phase change during coherent vibrational motion. This is often observed as an intensity node in the time-dependent Fourier spectra obtained from molecular bleach or stimulated emission signals.[31] We have not found evidence of these coherence nodes in our results. Therefore, the wavelength-independent dephasing lifetimes exceeding 1 ps agreed well with assignment of the coherent vibrational dynamics to mechanical acoustic modes rather than to a molecular-like wavepacket.

Finally, the relative initial phase obtained for multiple probe wavelengths is plotted in Figure 4c. A clear π-phase difference is observed for the excitation of GSB-675-detected (2.0 THz breathing mode) oscillations when compared to the signals obtained at shorter wavelengths where the 0.7 THz quadrupolar mode is dominant. This difference in excitation phase signifies two distinct mechanisms for launching the acoustic modes.[32] For larger nanoparticles, lattice anharmonicity is the most commonly observed mechanism for acoustic mode excitation. In this mechanism, rapid lattice heating following excitation causes the dilation of the particle, accompanied by successive expansion and contraction at the acoustic mode frequency. These lattice-induced vibrations are dominant when electron-to-lattice energy transfer (τ_{e-l}) is rapid compared to the vibrational period (T_{vib}), such that $T_{vib} > \tau_{e-l}$. When this situation is satisfied, the periodic intensity recurrences due to acoustic phonon modes typically show a sine-like dependence. However, when $T_{vib} \leq \tau_{e-l}$, as can be the case with ultrasmall gold nanoclusters, acoustic modes can also be launched by hot electron pressure. For hot-electron-pressure-induced oscillations, the intensity recurrences follow a cosine-like dependence. Hence, the two different acoustic mode excitation mechanisms are identified by a π-phase difference in the coherent vibrational signals. The π-phase shift observed between the two coherent vibrational signals reported here agrees well with their assignments to breathing (2.0 THz) and quadrupolar (0.7 THz) coherent acoustic modes. Given the approximate 1 ps electron−lattice energy

https://doi.org/10.1021/acs.jpclett.3c01477
J. Phys. Chem. Lett. 2023, 14, 6679−6685

transfer time constant and the 1.43 ps period of the quadrupolar mode, this vibration is likely excited by lattice-induced dilation. In contrast, the short (500 fs) period of the breathing mode is likely to have a significant excitation contribution from the hot electron pressure.

In summary, the coherent vibrational properties of $Au_{144}(SC_8H_9)_{60}$ have been described. Two coherent acoustic vibrations have been assigned and include a 2.0 THz radially symmetric breathing mode and a lower frequency 0.7 THz quadrupolar mode. Support for these assignments was obtained from the collective agreement of the vibrational mode frequencies, their size dependences (or independences), relative excitation phases, and the persistence of coherent recurrences over several picoseconds. The assignments were also supported by measurements of Ag-substituted $Au_{144}(SC_8H_9)_{60}$. The data were fully reconciled by the mechanical vibrations of the MPCs and did not require the use of molecular wavepacket models. The 2.0 THz breathing mode was size independent and exhibited a decoherence time of 1.75 ps; coherences persisting on the picosecond time scale were detected throughout the probe window. The 1.43 ps period of the 0.7 THz quadrupolar mode matched predicted expectations for the $Au_{144}(SC_8H_9)_{60}$ equivalent diameter of 1.67 nm. Based on these findings, the acoustic vibrations of $Au_{144}(SC_8H_9)_{60}$ are consistent with models based on continuum mechanics. The current results provide important information about the mechanical properties of $Au_{144}(SC_8H_9)_{60}$, which is a nanocluster species considered near the verge of metallicity. An interesting open question concerns why distinct acoustic modes are detected at select probe wavelengths. Understanding this state selectivity may be an interesting area for continued research.

■ ASSOCIATED CONTENT

Supporting Information

The Supporting Information is available free of charge at https://pubs.acs.org/doi/10.1021/acs.jpclett.3c01477.

> Experimental details and schematic of femtosecond transient absorption experiments, linear absorption spectra of Au_{144} nanoclusters and fitting functions, synthesis details for all nanoclusters studied, details for the calculated projected density of states and TCM analyses including relative contributions from gold, sulfur, and superatom states, transient absorption spectral and residual plots of coherent signals for $Ag_xAu_{144-x}(PET)_{60}$ nanoclusters, coherent vibrational dynamics of Au_{25} nanoclusters, and tabulated periods and frequencies of quadrupolar and breathing modes for nanoclusters of various D_{eq} (PDF)

■ AUTHOR INFORMATION

Corresponding Author

Kenneth L. Knappenberger, Jr. − *Department of Chemistry, Pennsylvania State University, University Park, Pennsylvania 16802, United States;* orcid.org/0000-0003-4123-3663; Email: klk260@psu.edu

Authors

William R. Jeffries − *Department of Chemistry, Pennsylvania State University, University Park, Pennsylvania 16802, United States;* orcid.org/0000-0002-4870-5910

Sami Malola − *Department of Physics, Nanoscience Center, University of Jyväskylä, Fl-40014 Jyväskylä, Finland*

Marcus A. Tofanelli − *Department of Chemistry, Colorado State University, Fort Collins, Colorado 80523, United States*

Christopher J. Ackerson − *Department of Chemistry, Colorado State University, Fort Collins, Colorado 80523, United States;* orcid.org/0000-0001-6863-6054

Hannu Häkkinen − *Department of Physics, Nanoscience Center, University of Jyväskylä, Fl-40014 Jyväskylä, Finland; Department of Chemistry, Nanoscience Center, University of Jyväskylä, Fl-40014 Jyväskylä, Finland;* orcid.org/0000-0002-8558-5436

Complete contact information is available at: https://pubs.acs.org/10.1021/acs.jpclett.3c01477

Notes

The authors declare no competing financial interest.

■ ACKNOWLEDGMENTS

This work was supported by a grant from the Air Force Office of Scientific Research (FA9550-22-1-0402). W.R.J. acknowledges support from the National Science Foundation, award CHE-1807999 and CHE-2204190. C.J.A. acknowledges support from the National Science Foundation, award CHE-1507646. Chongyue Yi and Hongjun Zheng are acknowledged for assistance with the transient absorption results. H.H. acknowledges support from the Academy of Finland. The DFT computations were made at the Finnish National Supercomputing Center, CSC.

■ REFERENCES

(1) Yang, Y. T.; Callegari, C.; Feng, X. L.; Ekinci, K. L.; Roukes, M. L. Zeptogram-Scale Nanomechanical Mass Sensing. *Nano Lett.* **2006**, *6* (4), 583−586.

(2) Portales, H.; Goubet, N.; Saviot, L.; Adichtchev, S.; Murray, D. B.; Mermet, A.; Duval, E.; Pileni, M. P. Probing Atomic Ordering and Multiple Twinning in Metal Nanocrystals Through Their Vibrations. *Proc. Natl. Acad. Sci. U.S.A.* **2008**, *105*, 14784−14789.

(3) Pelton, M.; Sader, J. E.; Burgin, J.; Liu, M.; Guyot-Sionnest, P.; Gosztola, D. Damping of Acoustic Vibration in Gold Nanoparticles. *Nat. Nanotechnol.* **2009**, *4*, 492−495.

(4) Dowgiallo, A. M.; Schwartzberg, A. M.; Knappenberger, K. L., Jr. Structure-Dependent Coherent Acoustic Vibrations of Hollow Gold Nanospheres. *Nano Lett.* **2011**, *11* (8), 3258−3262.

(5) Hartland, G. V. Measurements of the Material Properties of Metal Nanoparticles by Time-Resolved Spectroscopy. *Phys. Chem. Chem. Phys.* **2004**, *6*, 5263−5274.

(6) Hartland, G. V. Coherent Excitation of Vibrational Modes in Metallic Nanoparticles. *Annu. Rev. Phys. Chem.* **2006**, *57*, 403−430.

(7) Wheeler, D. A.; Green, T. D.; Wang, H.; Fernandez-Lopez, C.; Liz-Marzan, L.; Zou, S.; Knappenberger, K. L., Jr.; Zhang, J. Z. Optical Properties and Coherent Vibrational Oscillations of Gold Nanostars. *Chem. Phys. Lett.* **2012**, *543*, 127−132.

(8) Ostovar, B.; Su, M. N.; Renard, D.; Calrk, B. D.; Dongare, P. D.; Dutta, C.; Gross, N.; Sader, J. E.; Landes, C. F.; Chang, W. S.; Halas, N. J.; Link, S. Acoustic Vibrations of Al Nanocrystals: Size, Shape, and Crystallinity Revealed by Single-Particle Transient Extinction Spectroscopy. *J. Phys. Chem. A* **2020**, *124* (19), 3924−3934.

(9) Maioli, P.; Stoll, T.; Sauceda, H. E.; Valencia, I.; Demessence, A.; Bertorelle, F.; Crut, A.; Vallee, F.; Garzon, I. L.; Cerullo, G.; Del Fatti, N. Mechanical Vibrations of Atomically Defined Metal Clusters: From Nano- to Molecular-Size Oscillators. *Nano Lett.* **2018**, *18* (11), 6842−6849.

(10) Zhou, M.; Vdovic, S.; Long, S.; Zhu, M.; Yan, L.; Wang, Y.; Niu, Y.; Wang, X.; Guo, Q.; Jon, R.; Xia, A. Intramolecular Charge

Transfer and Solvation Dynamics of Thiolate-Protected $Au_{20}(SR)_{16}$ Clusters Studied by Ultrafast Measurement. *J. Phys. Chem. A* **2013**, *117* (40), 10294−10303.
(11) Zhou, M.; Zeng, C.; Song, Y.; Padelford, J. W.; Wang, G.; Sfeir, M. Y.; Higaki, T.; Jin, R. On the Non-Metallicity of 2.2 nm $Au_{246}(SR)_{80}$ Nanoclusters. *Angew. Chem., Int. Ed.* **2017**, *56*, 16257−16261.
(12) Zhang, W.; Kong, J.; Li, Y.; Kuang, Z.; Wang, H.; Zhou, M. Coherent Vibrational Dynamics of $Au_{144}(SR)_{60}$ Nanoclusters. *Chem. Commun.* **2022**, *13*, 8124−8130.
(13) Jin, R.; Zeng, C.; Zhou, M.; Chen, Y. Atomically Precise Colloidal Metal Nanoclusters and Nanoparticles: Fundamentals and Opportunities. *Chem. Rev.* **2016**, *116* (18), 10346−10413.
(14) Ingram, R. S.; Hosteler, M. J.; Murray, R. W.; Schaaff, G. T.; Khoury, J. T.; Whetten, R. L.; Bigioni, T. P.; Guthrie, D. K.; First, P. N. 28 kDa Alkanethiolate-Protected Au Clusters Give Analogous Solution Electrochemistry and STM Coulomb Staircases. *J. Am. Chem. Soc.* **1997**, *119* (39), 9279−9280.
(15) Yi, C.; Tofanelli, M. A.; Ackerson, C. J.; Knappenberger, K. L., Jr. Optical Properties and Electronic Energy Relaxation of Metallic $Au_{144}(SR)_{60}$ Nanoclusters. *J. Am. Chem. Soc.* **2013**, *135* (48), 18222−18228.
(16) Yi, C.; Zheng, H.; Tvedte, L. M.; Ackerson, C. J.; Knappenberger, K. L. Nanometals: Identifying the Onset of Metallic Relaxation Dynamics in Monolayer-Protected Gold Clusters Using Femtosecond Spectroscopy. *J. Phys. Chem. C* **2015**, *119* (11), 6307−6313.
(17) Zheng, H.; Tofanelli, M. A.; Ackerson, C. J.; Knappenberger, K. L., Jr. Composition-Dependent Electronic Energy Relaxation Dynamics of Metal Domains as Revealed by Bimetallic $Au_{144-x}Ag_x(SC_8H_9)_{60}$ Monolayer-Protected Clusters. *Phys. Chem. Chem. Phys.* **2017**, *19*, 14471−14477.
(18) Mustalahti, S.; Myllyperkiö, P.; Lahtinen, T.; Salorinne, K.; Malola, S.; Koivisto, J.; Häkkinen, H.; Pettersson, M. Ultrafast Electronic Relaxation and Vibrational Cooling Dynamics of $Au_{144}(SC_2H_4Ph)_{60}$ Nanocluster Probed by Transient Mid-IR Spectroscopy. *J. Phys. Chem. C* **2014**, *118* (31), 18233−18239.
(19) Foxley, J.; Knappenberger, K. L., Jr. Magneto-Optical Properties of Noble Metal Nanostructures. *Annu. Rev. Phys. Chem.* **2023**, *74*, 53−72.
(20) Foxley, J.; Green, T. D.; Tofanelli, M. A.; Ackerson, C. J.; Knappenberger, K. L., Jr. The Evolution from Superatom- to Plasmon-Mediated Magnetic Circular Dichroism in Colloidal Metal Nanoparticles Spanning the Nonmetallic to Metallic Limits. *J. Phys. Chem. Lett.* **2023**, *14* (22), 5210−5215.
(21) Jensen, K. M.Ø.; Juhas, P.; Tofanelli, M. A.; Heinecke, C. L.; Vaughan, G.; Ackerson, C. J.; Billinge, S. J. L. Polymorphism in Magic-Sized $Au_{144}(SR)_{60}$ Clusters. *Nat. Commun.* **2016**, *7*, 11859.
(22) Negishi, Y.; Zakazaki, T.; Malola, S.; Takano, S.; Niihori, Y.; Kurashige, W.; Yamazoe, S.; Tsukada, T.; Häkkinen, H. A Critical Size for Emergence of Nonbulk Electronic and Geometric Structures in Dodecanethiolate-Protected Au Clusters. *J. Am. Chem. Soc.* **2015**, *137* (3), 1206−1212.
(23) Lopez-Acevedo, O.; Akola, J.; Whetten, R. L.; Gronbeck, H.; Häkkinen, H. Structure and Bonding in the Ubiquitous Icosahedral Metallic Gold Cluster $Au_{144}(SR)_{60}$. *J. Phys. Chem. C* **2009**, *113* (13), 5035−5038.
(24) Yan, N.; Xia, N.; Liao, L.; Zhu, M.; Jin, F.; Jin, R.; Wu, Z. Unraveling the Long-Pursued Au_{144} Structure by x-Ray Crystallography. *Sci. Adv.* **2018**, *4*, No. eaat7259.
(25) Combe, N.; Saviot, L. Acoustic Modes in Metallic Nanoparticles: Atomistic Versus Elasticity Modeling. *Phys. Rev. B* **2009**, *80*, No. 035411.
(26) Saviot, L.; Murray, D. B. Acoustic Vibrations of Anisotropic Nanoparticles. *Phys. Rev. B* **2009**, *79*, No. 214101.
(27) Zhou, M.; Tian, S.; Zeng, C.; Sfeir, M. Y.; Wu, Z.; Jin, R. Ultrafast Relaxation Dynamics of $Au_{38}(SC_2H_4Ph)_{24}$ Nanoclusters and Effects of Structural Isomerism. *J. Phys. Chem. C* **2017**, *121* (20), 10686−10693.
(28) Knappenberger, K. L., Jr.; Lerch, E-B. W.; Wen, P.; Leone, S. R. Coherent Polyatomic Dynamics Studied by Femtosecond Time-Resolved Photoelectron Spectroscopy: Dissociation of Vibrationally Excited CS_2 in the *6s* and *4d* Rydberg States. *J. Chem. Phys.* **2006**, *125*, No. 174314.
(29) Knappenberger, K. L., Jr.; Lerch, E-B. W.; Wen, P.; Leone, S. R. Stark-Assisted Population Control of Coherent CS_2 *4f* and *5p* Rydberg Wave Packets Studied by Femtosecond Time-Resolved Photoelectron Spectroscopy. *J. Chem. Phys.* **2007**, *127*, No. 124318.
(30) Brazard, J.; Bizimana, L. A.; Gellen, T.; Carbery, W. P.; Turner, D. B. Experimental Detection of Branching at a Conical Intersection in a Highly Fluorescent Molecule. *J. Phys. Chem. Lett.* **2016**, *7* (1), 14−19.
(31) Rafiq, S.; Scholes, G. D. Slow Intramolecular Vibrational Relaxation Leads to Long-Lived Excited State Wavepackets. *J. Phys. Chem. A* **2016**, *120* (34), 6792−6799.
(32) Crut, A.; Maioli, P.; Del Fatti, N.; Vallee, F. Acoustic Vibrations of Metal Nano-Objects: Time-Domain Investigations. *Phys. Rep.* **2015**, *549* (1), 1−43.

https://doi.org/10.1021/acs.jpclett.3c01477
J. Phys. Chem. Lett. 2023, 14, 6679−6685